npj | materials degradation

Article

Published in partnership with CSCP and USTB

Article in Press

https://doi.org/10.1038/s41529-026-00912-7

Predicting Intergranular Corrosion Penetration Depth in Accelerated Testing using Machine Learning

Check for updates

David Montes de Oca Zapiain[1] ✉, Christoph Altenbach[2], Laura Kopruch[3], Aditya Venkatraman[1], Ryan M. Katona[1] & Daniela Zander[3]

Aluminum (Al) 6000 series alloys are relevant in automotive applications due to great strength, excellent machinability, formability, and good weldability. Nevertheless, aluminum alloys are susceptible to intergranular corrosion (IGC), making it crucial to determine the relationship that exists between the alloy composition and manufacturing parameters and the corresponding rate and magnitude of IGC observed. The large number of parameters that affect this behavior requires the development of a more robust framework. In this work, a probabilistic model is leveraged to establish an accurate linkage between a set of input parameters (e.g., alloying content and heat treatment) and the resultant IGC performance (i.e., penetration depth) of multiple Al 6000 series alloys. The model extracts usable knowledge from a curated database comprising 128 individual experimental results. The developed framework and established models are further validated by predicting the penetration depth of six new/unseen alloys.

The unique combination of properties from Al–Mg–Si(–Cu) alloys (6000 series), such as specific strength, excellent machinability, formability, and weldability, makes them relevant for automotive applications[1]. 6000 series aluminum alloys are commonly used as sheet materials in the outer skin, as well as for extrusions in structural parts and screws[1–3]. While these alloys exhibit adequate corrosion resistance, particularly with regard to stress corrosion cracking and hydrogen embrittlement[4,5], they can be susceptible to intergranular corrosion (IGC). IGC propagates rapidly, is difficult to detect with line-of-sight methods, and leads to reduced mechanical load capacity due to the formation of crack initiation sites[6,7].

The IGC susceptibility is determined not only by the operating environment, but also by multiple parameters such as the chemical composition, casting and solidification parameters, and the thermomechanical history[2,4,8–10]. For this reason, it is crucial to determine the influence of the various parameters in terms of the rate and magnitude of IGC observed in Al–Mg–Si(–Cu) alloys.

Experimental efforts have observed various trends in the IGC behavior of 6000 series aluminum alloys. For example, IGC susceptibility has been correlated to multiple distinct mechanisms, including grain boundary precipitation (Q-$Al_5Cu_2Mg_8Si_6$, β-Mg_2Si)[2,10–14], precipitate-free zones and element depletion zones (Mg, Si, and Cu)[4,13–18], as well as element enrichment (Cu and/or Si)[10,11,15,19,20]. Besides the direct initiation at susceptible grain boundaries, IGC can also be initiated by the exposure of susceptible grain boundaries through pitting corrosion, which results from the local dissolution of the surrounding aluminum matrix caused by the cathodic oxygen reduction reaction (ORR) at intermetallic particles, such as Fe-rich phases[21,22].

Experiments have also enabled the development of a fundamental understanding of the effect that different alloying elements have on the resultant IGC susceptibility[23,24]. For example, it has been reported that the Mg to Si ratio is a determining factor in Cu-lean aluminum alloy's susceptibility to IGC[11,19]. This can be attributed to the presence of excess Si that is not bound within the precipitates. This excess Si has the tendency to segregate to the grain boundaries, resulting in an anodic behavior of the Si-depleted precipitate-free zone (PFZ) adjacent to the Si-enriched grain boundaries[11,19]. However, Cu-lean alloys are mostly reported as resistant to IGC[10], while Cu-rich alloys are susceptible to IGC even after short-term artificial aging[3,10]. In Cu-rich alloys, the IGC susceptibility has been related primarily to the Cu content and, secondarily, to the Mg/Si ratio, whereby excess Mg can improve the IGC resistance[23].

Similar relationships have also been observed between the severity of IGC and the heat treatment (HT) to which the alloy was exposed. Conditions such as T6 (peak-aged condition using artificial aging), and T4 (solution annealed, quenched, and naturally aged), have a significant effect

[1]Sandia National Laboratories, 1515 Eubank Blvd SE, Albuquerque, 87123 NM, USA. [2]Institute for Frontier Materials on Earth and in Space, German Aerospace Center (DLR), Linder Höhe, Cologne, 51147 NW, Germany. [3]Chair of Corrosion and Corrosion Protection, RWTH Aachen University, Intzestr. 5, Aachen, 52072 NW, Germany. ✉e-mail: dmonte@sandia.gov

on the observed IGC behavior[2,3]. The effect of overaging and underaging on the resultant behavior has also been analyzed[3,17]. Previous work showed that the susceptibility of Cu-containing alloys to IGC in the "underaged" and T6 conditions is explained by the formation of a Cu nanofilm at the grain boundary, which has a cathodic effect on the surrounding Cu-depleted PFZ[12,16]. It has also been mentioned that with increasing aging to the overaged state, the Cu diffuses into the Q-phases at the grain boundary, whereby galvanic coupling of the Q-phase with the Cu-depleted PFZ becomes the dominant mechanism[10,12,20,25]. Moreover, it has been shown that dispersoid-forming elements such as Cr, Mn, Zr, Sc, or V have a significant impact on the grain aspect ratio of the Al–Mg–Si(–Cu) alloys[1,26–28]. These elements effectively suppress recrystallization and promote the formation of subgrain boundaries during the forming process. Hence, the segregation of Mg, Si, and Cu is reduced due to a greater number of potential nucleation sites. Consequently, less continuous coverage of high-angle grain boundaries with precipitates is expected, leading to a less predetermined corrosion path.

It can be seen that experimental analysis is critical for establishing insights and developing a fundamental understanding of the relationship between the inputs and outputs for IGC. Nevertheless, these insights require many experiments that are complex and capital-intensive. Consequently, the cost and time required to perform these experiments throttle the number of experiments that can be performed. Therefore, in cases when multiple variables are evaluated, experiments yield insights and correlations that can be leveraged as heuristic design rules, aiding in the selection of a material, but fail to provide an estimation or prediction of the extent of IGC that can occur. Thus, in order to evaluate the specific performance of an alloy, a variety of standardized accelerated corrosion tests must be performed[29]. Evaluating the performance of each alloy using experimental tests, even if accelerated, represents an additional challenge as the results of these tests are not often comparable to the end application[21,30]. Furthermore, given the open parameterization of certain standards, a broad range of input parameters can satisfy the requirements [29–31]. This results in variability in the IGC susceptibility of an alloy and can complicate the comparison and transfer of results between different laboratories or testing procedures. Consequently, a new iteration of experiments is required each time a new alloy or parameter needs to be evaluated. Therefore, a more robust and efficient framework for assessing the IGC performance of alloys is crucial.

Machine learning (ML) is a viable solution for establishing the desired framework given its ability to establish accurate and robust linkages between inputs and outputs that exhibit complex and non-linear behavior[32]. Furthermore, it has been successfully leveraged for corrosion characterization and prediction in the past[33–36].

Li et al.[37] and Feng et al. [38] demonstrate that ML can be successfully applied for providing a prediction of the IGC performance of an Al–Mg–Si alloy (i.e., penetration depth), and that the results can be further utilized as a design tool. Sheik et al.[39] leveraged ML to predict the degree of sensitization (DOS) from a set of experimentally obtained measurements, while Falaakh et al.[40] extracted knowledge from a database of crack growth rates. In general, ML models can extract usable knowledge from previously obtained IGC results. However, these existing applications do not have the capability to evaluate the uncertainty associated with the predictions, given the fact that they have been implemented leveraging deterministic models. Falaakh et al.[40] point out that this capability can be incorporated by employing boosting (i.e., model ensembling[41]). Nevertheless, the state-of-the-art implementations showcase that a systematic knowledge extraction protocol capable of providing not only a prediction but rather a distribution of predictions for a given set of inputs for the IGC performance of Al–Mg–Si(–Cu) alloys still needs to be developed/implemented.

In this work, the aforementioned gap is addressed by leveraging probabilistic models to establish an accurate linkage between a set of input parameters (e.g., alloying content and heat treatment) and the resultant IGC performance (i.e., penetration depth) of multiple Al–Mg–Si(–Cu) alloys. To achieve this, a database of the penetration depth of 128 data points for multiple alloys was curated from previously published work[2–4,29,30,42]. Subsequently, following previous successes[43], Gaussian Processes (GPs), which are a type of probabilistic models[44], were utilized to connect the set of inputs to the obtained penetration depth. Finally, the created model was validated by using it to predict the maximum penetration depth of a completely separate set of data comprised of three new alloys procured for this work, as well as three distinct alloys whose performance was characterized in previous work[8,9].

Results

Experimental analysis

A database of results from previously published work was curated[2–4,29,30,42] that comprised distinct variables, such as alloying content and heat treatment, and the resultant penetration depth for Al–Mg–Si(–Cu) alloys. The heat treatment conditions considered are T4 and T6, as well as a condition that simulates the heat exposure during the painting stage in automotive manufacturing, referred to as bake hardening (BH). The latter can be regarded as an underage condition. Further variables that were considered result from the standardized testing procedure according to the ISO 11846 Method B[31]. Overall, the database contains 128 separate data points, and the specific variables analyzed with the experiments are detailed in Table 1. Each data point represents the average and standard deviation of 30 penetration depths, given that three samples were examined for each parameter variation, and two cross-sections were examined for each sample; then, for each cross-section examined, the five largest penetration depths were recorded.

A preliminary analysis of the database was performed by plotting the values of the penetration depth against the values of the distinct variables recorded and colored by heat treatment, shown in Fig. 1. While some qualitative trends exist in the scatter plots (Fig. 1), it is quite complicated to extract precise trends. For example, from Fig. 1a, a general trend of increasing penetration depths as the % of Cu increases can be observed. However, the trend is limited since a broad dispersion of penetration depth values is observed at the same Cu content. In other cases (Fig. 1g), a trend is not apparent as similar penetration depths are associated with distinct values of temperature.

Although trends are not immediately visible, this does not imply the absence of a relationship between the distinct variables and the penetration depth. It potentially indicates that the relationship is complex, given the high dimensionality of the space, and most likely non-linear. Consequently, conventional analysis is limited in extracting qualitative insights from the vast amount of information present. This underscores the importance of implementing ML-based techniques for building linkages between the inputs and outputs.

Knowledge extraction using Gaussian processes

A computationally efficient linkage between the input parameters and the resultant IGC performance of the collated experimental data using Gaussian

Table 1 | Experimental variables and their corresponding types

Parameter	Type of variable
Cu [wt%]	Continuous (numeric)
Mg [wt%]	Continuous (numeric)
Si [wt%]	Continuous (numeric)
HT condition	Categorical
Volume/surface area [ml/cm^2]	Continuous (numeric)
$T_{electrolyte}$ [°C]	Continuous (numeric)
$t_{pretreatment}$ [min]	Continuous (numeric)
$T_{pretreatment}$ [°C]	Continuous (numeric)
$HNO_{3\ pretreatment}$ [ml/l]	Continuous (numeric)
$HF_{pretreatment}$ [ml/l]	Continuous (numeric)
$NaOH_{pretreatment}$ [ml/l]	Continuous (numeric)
Storage time [d]	Continuous (numeric)

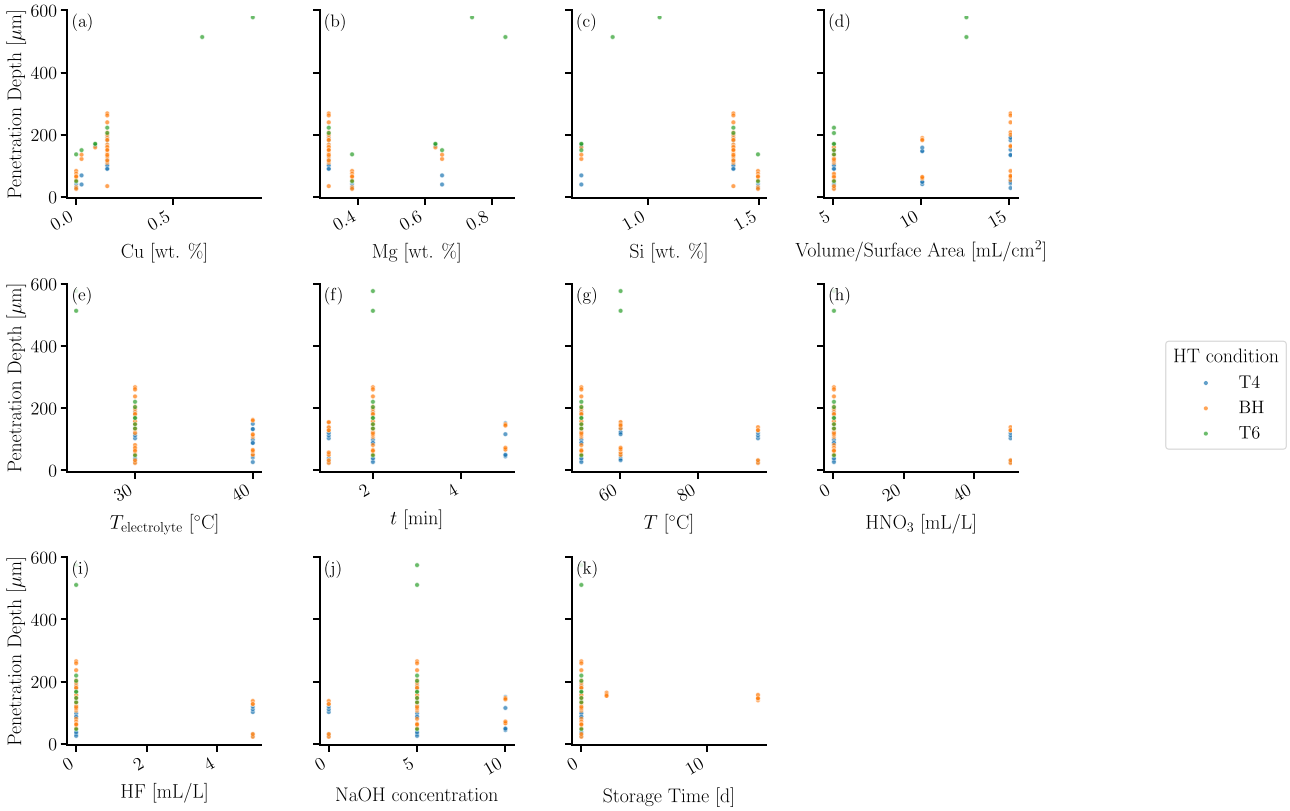

Fig. 1 | Scatter plots for each of the distinct input variables vs. the penetration depth for the compiled experimental results colored by heat treatment: T4 (solution annealed, quenched and naturally aged); T6 (peak aged); BH (bake hardened/underaged. a Penetration depth [μm] vs. Cu [wt%]. **b** Penetration depth [μm] vs. Mg [wt%]. **c** Penetration depth [μm] vs. Si [wt%]. **d** Penetration depth [μm] vs. volume/surface area [ml/cm^2]. **e** Penetration depth [μm] vs. $T_{electrolyte}$ [°C]. **f** Penetration depth [μm] vs. $t_{pretreatment}$ [min]. **g** Penetration depth [μm] vs.$T_{pretreatment}$ [°C]. **h** Penetration depth [μm] vs. $HNO_{3\ pretreatment}$ [ml/l]. **i** Penetration depth [μm] vs. $HF_{pretreatment}$ [ml/l]. **j** Penetration depth [μm] vs. $NaOH_{pretreatment}$ [ml/l]. **k** Penetration depth [μm] vs. storage time [d].

Processes Regression (GPR) models[44] was created. In this work, the set of inputs contains a mixture of categorical and continuous values as detailed in Table 1. The output corresponds to the penetration depth in μm. Following standard practice, feature engineering was performed on the inputs and outputs. Categorical variables were transformed using a One-Hot Encoder and then subsequently normalized to the [0, 1] domain. In a similar manner, the output values were normalized to the [0, 1] domain. These transformations and normalizations were applied using SciKit Learn[45].

The experimental data has inherent uncertainty that is captured by using a mean penetration depth and its corresponding standard deviation of 30 measurements. Naturally, the standard deviations of the distinct captured measurements are not homogeneous. To account for the variability of the uncertainty across the distinct experiments, two distinct GPR-based models were used: one that predicts the penetration depth and the second that predicts the estimated variability associated with that prediction.

As a result, the GPR-based model that predicts the penetration depth also provides an associated variability, but that variability is solely related to the model itself (i.e., epistemic uncertainty), while the GPR-based model that provides the estimated variability accounts for the variability that is observed directly from the experiments (i.e., aleatoric uncertainty). This decomposition captures not only the effect the distinct inputs have on the outputs but also on their corresponding variability[46,47].

To ensure that the models are capable of generalizing and are not overfitted, the Training Data contained 80% of the data available, randomly sampled, while the remaining 20% was used as the Validation Data. Figure 2 shows the penetration depth for the training and the validation sets. To facilitate interpretability, all the results are reported in the unnormalized domain. Figure 2 further shows that the training data encompasses the validation data and that the validation data is distinct from the training data.

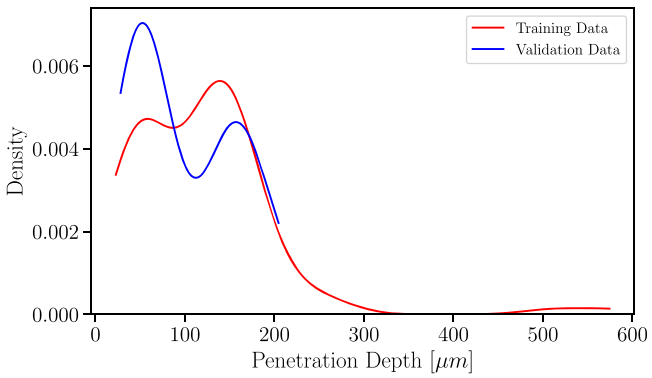

Fig. 2 | Distribution of the recorded penetration depth in μm for the training and testing datasets. Probability density distribution of the penetration depth μm, colored in red for the training set and in blue for the testing set.

This indicates that the validation data can be utilized to evaluate the performance of the model to predict new/unseen inputs.

The GPR-based model for predicting penetration depth uses a Matérn-5/2 kernel and has a zero mean function[44]. The parameters for this model were fitted by maximizing the log marginal likelihood[44]. To enhance the model fitting process, a multi-start optimization strategy was employed. This strategy performs multiple random initializations of the model parameter values that are then optimized using maximum likelihood estimation (MLE) and proceeds to select the best-performing model of all the performed initializations, which is the one that exhibits the lowest negative log marginal likelihood. For this work, 50 distinct initializations were

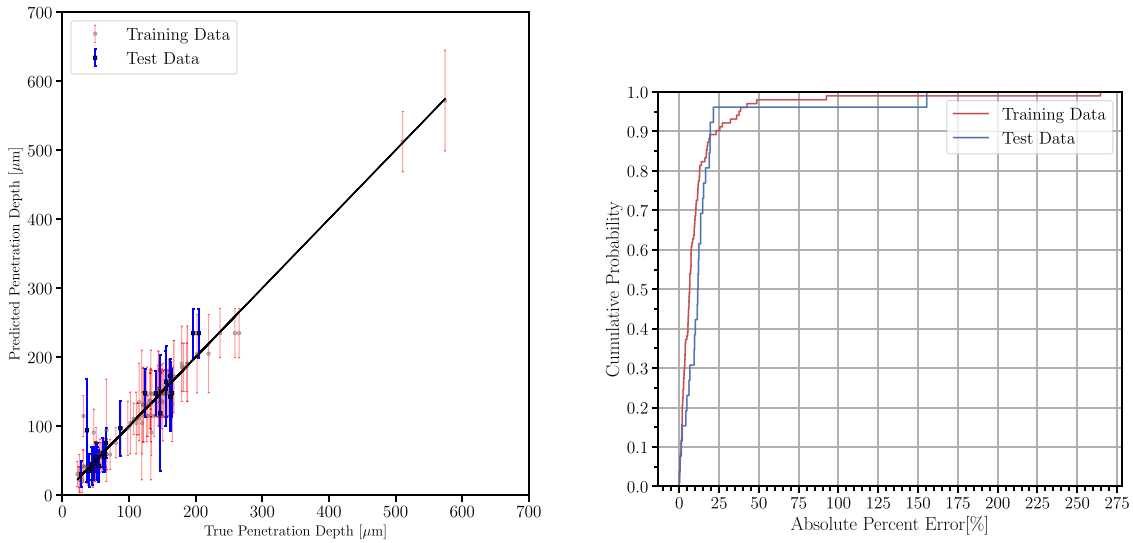

Fig. 3 | Gaussian process regression (GPR) based model performance plots. a Scatter plot of the predicted vs. true penetration depth values (in μm) with two standard deviations as the error bars. **b** Cumulative distribution of the absolute percent error for the Training and the Testing datasets.

performed. *GPflow*[48] was used for performing the described model-fitting protocol.

A similar process for fitting the GPR-based model that predicts the experimental variability was used. Note that the output of this second model is the experimental variance, which was obtained by taking the square of the reported experimental standard deviation, denoted by σ_{exp}. The experimental variance is thus denoted by σ^2_{exp}. To enable a better model fitting process, the range of observed variance was normalized to the [0, 1] domain, which we denote as $\hat{\sigma}^2_{exp}$. To ensure that the variance is always positive, the following transformation was applied:

$$\hat{\sigma}^2_{\text{exp}_t} = \log\left(1 + \hat{\sigma}^2_{\text{exp}}\right). \tag{1}$$

As a result, the second model was fitted on the transformed variance denoted by Eq. (1). A Rational Quadratic kernel with a constant mean function was used for the experimental variability GPR-based model. Similar to the penetration depth GPR-based model, the uncertainty GPR model was fitted using MLE and a multi-start optimization strategy with 50 distinct initializations using *GPflow*. The total variance was calculated by adding the prediction of experimental variability GPR-based model to the uncertainty prediction obtained by the penetration depth GPR-based model as follows:

$$\sigma^2_{\text{total}}(x) = s^2_{\text{GP}}(x) + \hat{\sigma}^2_{\text{exp}}(x), \tag{2}$$

where $s^2_{\text{GP}}(x)$ is the variance predicted by the penetration-depth GP. Also, recall that the variability GPR-based model was trained on a scaled and log-transformed variance target (cf. Eq. (1)). Therefore, before adding $\hat{\sigma}^2_{\text{exp}}$ to the variance predicted by the penetration-depth GP, $\hat{\sigma}^2_{\text{exp}_t}$ was inverse-transformed and un-normalized.

The plots in Fig. 3 showcase the performance of the developed computationally efficient linkage established by the two GPR-based models. Specifically, Fig. 3a shows the true vs. predicted scatter plot of the established linkage. The scatter points correspond to the mean value of the penetration depth predicted using the penetration depth GPR-based model, and the error bands correspond to two standard deviations of the total variance, which were obtained by taking the square root of $\sigma^2_{\text{total}}(x)$. The predicted values lie close to the diagonal line, indicating that the predictions are accurate. A majority of the points on the diagonal line are within two standard deviations of the total predicted variance, showcasing that the model's uncertainty has high empirical coverage within two standard deviations. We additionally report the numerical values of the empirical coverage probability, which correspond to 92% for one standard deviation and 96% for two standard deviations on the training data. The values of the test data are 84% for one standard deviation and 100% for two standard deviations.

Finally, Fig. 3b shows the cumulative distribution of the absolute percent error, and roughly 90% of the predictions for the training and test data have an error less than 25%. Both of these plots showcase the accuracy of the fitted models. Finally, the mean absolute percent error (MAPE) is 12.3% for the training data and 16.2% for the test data; these numbers show that, despite a small overfit, the model is overall capable of generalizing to new/unseen scenarios. This observation is also supported by the similar behavior of the model in the two distinct sets showcased in Fig. 3a, b. We additionally report that the mean absolute error (MAE) is 9.04 μm for training data and 12.99 μm for test data, further complementing the percent error analysis.

Predicting the penetration depth of a new dataset using the extracted knowledge

To further demonstrate the validity and efficacy of the trained models, a new set of unseen conditions was curated and developed. This new unseen conditions dataset is comprised of three new alloys procured and evaluated in this work, as well as three alloys generated and analyzed in previously performed work[9].

The first three new alloys are Al–Mg–Si(–Cu) model alloys with a decreasing amount of copper. The copper weight percentages of the model alloys labeled MA1, MA2, and MA3 are 0.59 wt% Cu, 0.35 wt% Cu, and 0.16 wt% Cu, respectively. These alloys are denoted with triangles in Fig. 7a. It is pointed out that the effect of the heat treatment was evaluated on the MA's by performing experiments on the material in T4 and T6 conditions, meaning that six distinct conditions were evaluated. For each of these conditions, three samples were generated on which independent experiments were performed. Subsequently, from each one of these experiments, the five deepest penetration depths across one cross section were recorded. We computed the average and the standard deviation of these 15 deepest penetration depth measurements to assess the model. As a result, from these

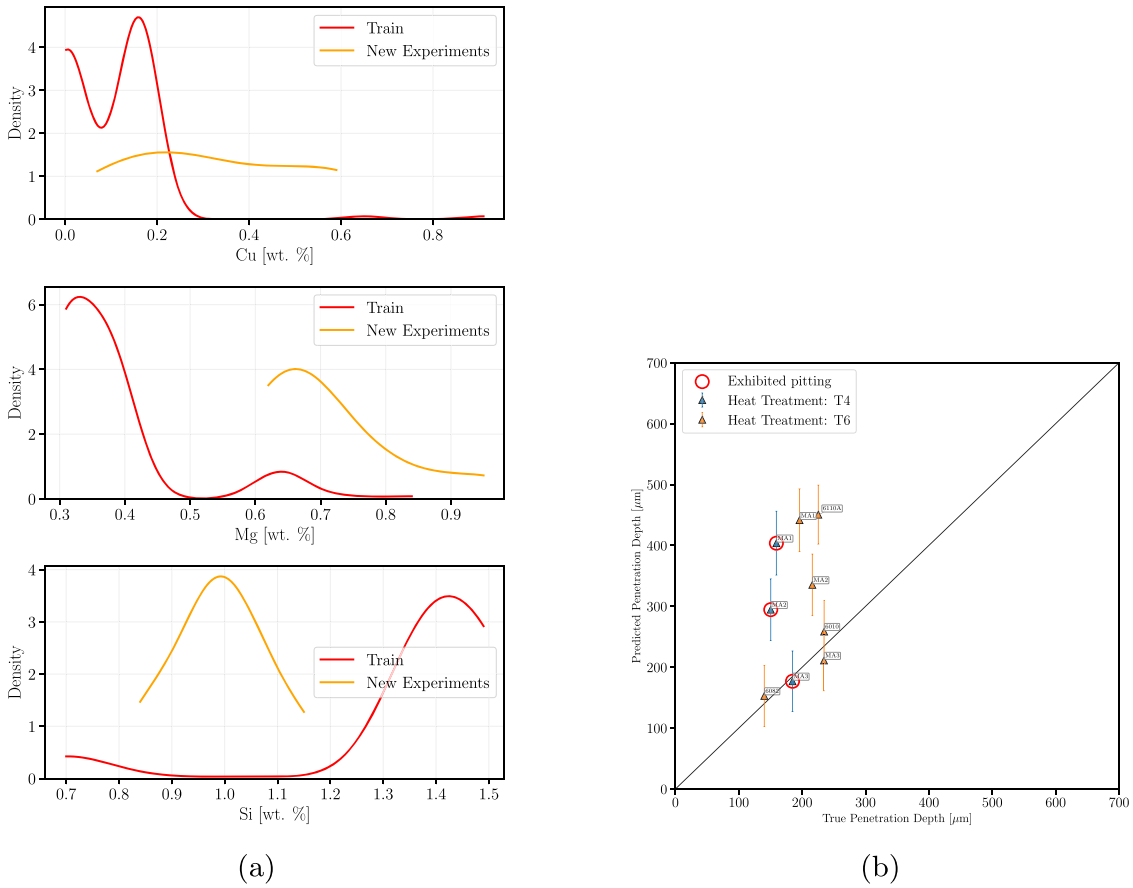

Fig. 4 | Unseen conditions dataset performance plots. a Probability density distribution plots of the distinct alloying components for the Training Data and the unseen conditions dataset. **b** Scatter plot of the predicted vs. true penetration depth values (in μm) with two standard deviations as the error bars for the unseen conditions dataset colored by heat treatment.

new alloys, we obtained six new average penetration depths and standard deviations.

The other set of three alloys investigated is 6082, 6110A, and 6010, and their specific composition is highlighted in Fig. 7a with labeled triangles[9]. These alloys were evaluated in the T6 condition, and double confirmation for each one of those alloys was performed. For each one of them, the five deepest penetration depths were recorded. The average and standard deviation over these ten penetration depth measurements per condition were computed to evaluate the trained model. Therefore, from this set of three alloys, we obtained three new averaged penetration depths and standard deviations.

A total of nine new unseen conditions and their corresponding performance are included in this dataset. It is important to point out that none of these conditions are present in the training data and, as such, are a valid set of new points to critically evaluate the performance of the model in new scenarios. This dataset is referred to as the unseen conditions dataset.

Figure 4a shows the composition details of the unseen conditions evaluated in the experiments using probability density distribution plots. From Fig. 4a, it is clear that the unseen conditions are evaluating a distinct area of composition space. Although the compositions are not included in the training set, the unseen conditions are mostly comprised of the limits of the training data, as only a tiny fraction of the data explores a Mg weight percentage that is outside of the training regime. However, the model requires 13 distinct inputs, which means that this is a 13-dimensional space that cannot be trivially visualized. Moreover, these inputs are from quite distinct feature spaces. Therefore, in order to quantitatively determine how separate the unseen conditions are from the training data, we projected the 13 dimensions to a new set of orthogonal axes that capture the variance of the data in ascending order using principal component analysis (PCA)[49].

PCA is a linear and distance-conserving transformation that enables us to calculate the distance from the training data to the nine separate unseen conditions evaluated. PCA was fitted to the Training data to obtain an orthogonal set of 13 dimensions, and the nine unseen conditions were projected to this new space. The mean nearest neighbor distance between the training data and the nine unseen conditions is 0.57. For comparison, the mean nearest neighbor distance between the training data and the test data is 0.036. Therefore, the conditions evaluated with these nine unseen alloys are quite distinct and separate from the training data.

Lastly, we used the first three PC dimensions, remember that these capture the variance of the data in ascending order, to define a convex hull and determined that six of the unseen conditions are outside of the convex hull defined by the training data. Thus, implying that the model is most likely extrapolating in these conditions. Three of the unseen conditions are inside the convex hull defined by the training data, which means that the model is most likely interpolating. Figure 4b showcases the performance of the model on the unseen conditions, plotting the value predicted with the model against the true penetration depth value obtained experimentally. As illustrated in Fig. 4b, the model has notable accuracy in predicting the experimental values for 6082, MA3 (for both heat treatments), and 6010 to the fitted line. However, in other cases, the model overpredicted the penetration depth to a significant extent, regardless of the heat treatment condition. The average error metrics for the predictions on the unseen conditions are 116.21 μm for the MAE and 62.5% for the MAPE.

For predictions related to corrosion damage, an overprediction from the model is preferred, as it leads to over-engineering and overestimation of damage rather than early failure, which can be catastrophic. Despite this, the fact remains that for some unseen conditions, the model estimated a drastically higher penetration depth than was recorded from the experiment.

Analyzing the composition of the unseen conditions, it is noticed that the alloys for which the model overpredicted have a copper content that is greater than 0.22 wt% Cu. This information is obtained from the legend in Fig. 4b and the composition chart shown in Fig. 7a. Additionally, as displayed in Fig. 1a, the higher copper content typically corresponds to higher values of penetration depth. Therefore, the model is qualitatively behaving as expected, given that it is displaying the trend captured by the training data. However, the unseen conditions did not exhibit that trend. As noted in Table 4, the MA's have similar Mg/Si ratios but decreasing Cu content, with MA1 having the highest Cu and MA3 having the lowest Cu content. Experimentally, all MAs had a similar true penetration depth (Fig. 4b). This is also noted in 6110A and MA1 in Fig. 4b, as both alloys contained a Cu content greater than 0.57 wt%.

Table 2 | Table detailing the percent error and the distance for the new alloys, distinguishing whether the alloys are inside the convex hull or outside the convex hull of the training data

Alloy	HT	Percent error (%)	Nearest neighbor distance in PC space
Inside the convex hull			
MA3	T4	4.27	0.3977
MA2	T4	95.76	0.4492
MA1	T4	153.33	0.6387
Outside the convex hull			
MA3	T6	9.94	0.3977
MA2	T6	55.16	0.4492
6082	T6	8.96	0.5746
MA1	T6	125.38	0.6387
6110A	T6	99.80	0.6902
6010	T6	10.17	0.9011

Table 2 provides detailed information about the percent error for each one of the unseen conditions as well as their nearest neighbor distance in PC space, while making a distinction if it is inside or outside the convex hull of the training data. The conditions are sorted by distance, and it is clearly seen that the model performance (i.e., error value) is not correlated to the distance from the training set, given that we see the condition that is farthest apart yield a prediction with a low value of percent error. This means that the model is unable to provide accurate predictions regardless of whether it is interpolating or extrapolating. Therefore, it is likely that another mechanism or cause is responsible for the decrease in performance.

In order to uncover this, the microstructure of the unseen conditions was analyzed. Fig. 5 shows the Barker-etched light microscopy images of the grain structure of the model alloys. Electrolytic Barker etching is a process that reveals the grain structure of aluminum alloys under a polarized light microscope. During the Barker etching process, a layer of oxide is formed, the thickness of which varies depending on the grain orientation[50]. This variation in thickness alters the reflectivity for certain wavelengths under polarized light, thereby enabling the distinction of individual grains. Images have been taken from the material in T4 condition in each sheet direction to gain a more comprehensive understanding of the rolling texture of the sheet material. The additional artificial heat treatment to the T6 condition will not change the grain size, since the temperature is below the recrystallization temperature of the alloys[9,51]. Thus, only the T4 condition was analyzed. As shown in Figure 5, the grains of the model alloys are elongated in the rolling direction (L). The elongation of the grains in the rolling direction increases

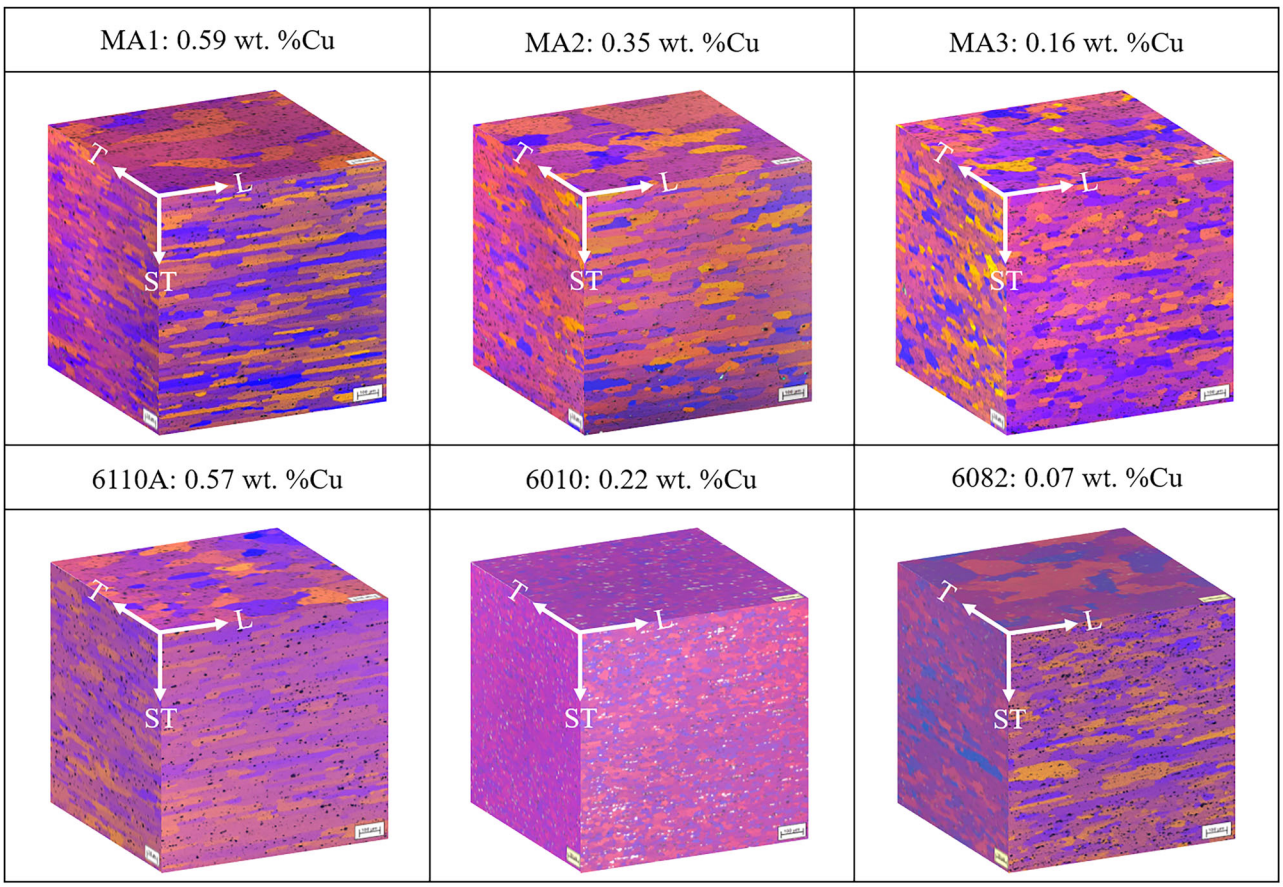

Fig. 5 | Highlight of the grain structure, obtained using Barker etched light microscopy, of the Model Alloys (MA's) and 6XXX alloys of the unseen conditions dataset. Barker etched light microscopy images of the grain structure of the MA's (MA1–MA3) and 6XXX alloys evaluated with the unseen conditions dataset.

with the Cu content. Simultaneously, the grains become narrower in the short transverse (ST). This can be proven by the grain aspect ratio obtained using EBSD analysis in Tables 3 and 4. The grain aspect ratio increases with the Cu content of the MA's, thereby deviating from the equiaxial ratio of 1. For 6010 and 6082, the model prediction demonstrates an accurate predicted penetration depth. It is noted that these alloys exhibited a maximum content of 0.22 wt% Cu. However, for 6110A (0.57 wt% Cu), the deviation is found to be significant and is similar in performance to MA1. It can also be observed from Fig. 5 and from the grain aspect ratios (Table 3) that the grains of the 6110A are elongated in the rolling direction (L).

As a result, in the present study, systems that have only slightly elongated grains or are more equiaxial (MA3, 6082, and 6010; Fig. 5) are correctly predicted by the GP model (Fig. 4). However, when more elongated grains are present (MA2, MA1, and 6110A; Fig. 5), the GP model overpredicts damage (Fig. 4).

In addition to the distinct grain structure and size, the corrosion mechanism is fundamentally different in some of the new alloys. Figure 6 shows representative light microscopy images of the corrosion morphology of the model alloys in T4 and T6 heat treatments, respectively. The alloys exhibit pitting corrosion or a mixture of severe pitting corrosion with minor IGC in the T4 condition and IGC in the T6 condition. With artificial aging, the mechanism switches from pitting to IGC.

It is important to acknowledge that the curated database solely contained experimental results relating to IGC. Thus, the model has not been exposed, nor trained to predict the damage caused by pitting corrosion. This represents another reason for the drastic reduction in accuracy from the previously trained model. It cannot be expected for the model to be able to generalize to new mechanisms if the model has not been trained on such examples, because this model will provide valid responses for the penetration depth caused by IGC. Acknowledging this, we report the performance of the model distinguishing by corrosion mechanism on the unseen conditions dataset. The unseen conditions that exhibited pitting had an MAE of 132.10 μm and a MAPE of 84.4%. The performance of the model on the unseen conditions that exhibited IGC corresponds to an MAE of 108.26 μm and a MAPE of 51.5%.

In conclusion, our model will be capable of providing accurate estimations of penetration depth in scenarios where IGC is the dominant corrosion mechanism and in cases where the underlying microstructure (i.e., grain size) does not present elongated grains.

Table 3 | Area-weighted grain aspect ratio of the LxST plane, evaluated by EBSD analysis and based on the Barker etched images for the MA's and the standardized alloys, respectively

Alloy	Cu content [wt%]	Grain aspect ratio
MA1	0.59	5.56
MA2	0.35	4.39
MA3	0.16	3.75
6110A	0.57	5.53
6010	0.22	1.69
6082	0.07	3.55

Table 4 | Chemical composition of the main alloying elements of 6000 series materials considered for the machine learning approach in wt%

Alloy	Mg	Si	Cu	Ref.
AA6016-High Cu	0.31	1.38	0.162	29,30
AA6016-Low Cu	0.38	1.49	0.002	29,30
AA6014-High Cu	0.63	0.7	0.1	30
AA6014-Low Cu	0.65	0.7	0.03	30
AA6056-High Cu	0.74	1.05	0.91	2,42
AA6056-Low Cu	0.84	0.84	0.65	3,4
AA6010	0.95	1.15	0.22	8,9
AA6110A	0.73	0.84	0.57	9
AA6082	0.81	0.89	0.07	9
MA1	0.68	1.06	0.59	
MA2	0.65	0.99	0.35	
MA3	0.62	0.97	0.16	

Discussion

The presented results demonstrate that GPR-based models are capable of distilling usable knowledge from previously obtained experimental results. Additionally, the probabilistic nature of GPR allowed for an adequate treatment of the variability by accounting for the epistemic uncertainty as well as the aleatoric uncertainty. This capability is considered to be of significant value, since it can later be adequately leveraged to guide where to perform other experiments. The calibrated uncertainty can be applied as a criterion to determine the necessity for new experimentation. Thus, enabling a data-driven procurement of knowledge.

The results shown also highlighted that the distilled knowledge was capable of being generalized to new/unseen alloys, as the trained model was

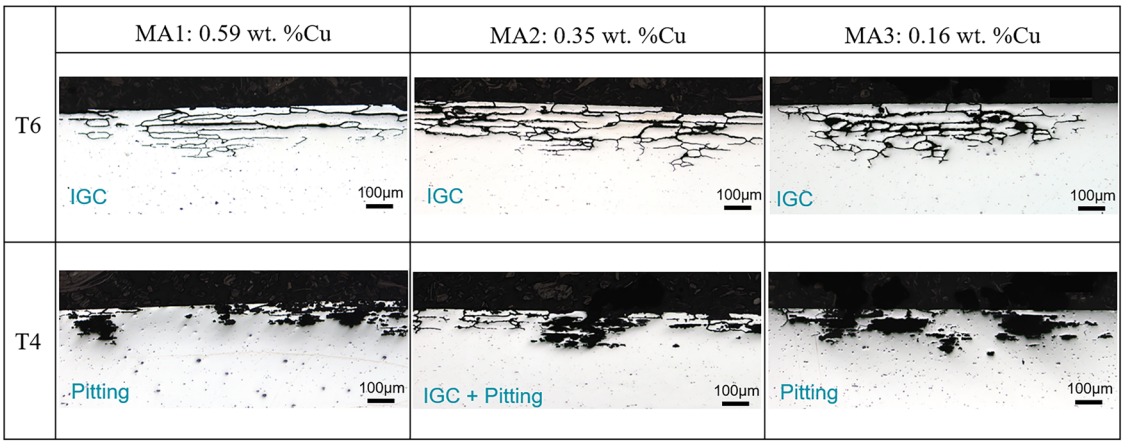

Fig. 6 | Demonstration of the switch in corrosion mechanism from pitting towards IGC with artificial aging on the Model Alloys (MA's) using light microscopy. Representative light microscopy images of the corrosion morphology in T4 and T6 conditions, showing a switch in corrosion mechanism from pitting towards IGC with artificial aging for the MA's.

able to provide accurate estimations of the penetration depth for some of the new model alloys analyzed in this work. It should be noted that the results of the model also indicated that it was not possible to provide accurate predictions for all of the alloys. Nevertheless, the decrease in performance and accuracy of the prediction was not caused by the GPR-based model itself.

The discrepancy between the behavior of the new alloys and the behavior recorded in the compiled and curated database was caused by the fact that the new alloys exhibited distinct microstructures (Fig. 5). Lervik et al.[52] have previously reported that IGC tends to occur mostly along the high-angle grain boundaries (HAGB's). In order to ensure the most comprehensive evaluation, only misorientation angles >15° have been considered in the calculations of the grain aspect ratios in this study. EBSD measurements of the MA's L × ST planes have revealed an increasing area-weighted average grain aspect ratio with increasing Cu content of the alloy, as demonstrated in Table 3. The grain aspect ratios indicate that the elongation of the MA's grains in the rolling direction increases with increasing Cu content, which is consistent with what the Barker etched images show (Fig. 5). This elongation leads to a longer total corrosion path length along the HAGB's, with a smaller penetration depth towards the center of the sample. Therefore, it can be concluded that the reduced penetration depth is directly correlated to the elongated grains that are perpendicular to the penetration depth measurement. Having said this, the trained model is unable to account for these critical parameters given the fact that the curated experimental database of results did not provide (or did not record) details regarding the grain morphology at the microscale. This limitation of the trained model could also be caused by the fact that the complete chemical composition of the alloys was not considered for model building. Especially, since some elements are related to the promotion (or prevention) of recrystallization (or recovery) of 6000 series alloys during thermomechanical processing and as such significantly influence the grain aspect ratio[53]. For instance, dispersoid-forming elements such as Zr, Cr, Mn, Sc, or V can increase the grain aspect ratio by retarding or preventing recrystallization, thereby limiting the availability of short corrosion pathways along HAGB's into the depth. In contrast, Fe and unbalanced levels of Mn, Cr, Cu, and Si can lead to the formation of coarse intermetallic particles that can further promote particle-stimulated nucleation and consequently recrystallization[1,26–28,53,54]. As a result, using more detailed information on thermomechanical processing, focusing particularly on the forming parameters and homogenization treatments, can also help overcome some of these limitations given their influence on the recrystallization behavior.

Additionally, it was observed that some cases of over-prediction of penetration depth by the model were cases that exhibited pitting corrosion. Pitting corrosion is a fundamentally different mechanism from IGC, which was observed in the database. This is clearly demonstrated in Fig. 6, which shows that pitting corrosion occurred in these cases, rather than the IGC behavior that was captured by the curated database. Pitting in Al-alloys occurs at (or at the interfaces of) second-phase particles—where the protective passive film is different[55,56]. Further, the galvanic coupling between cathodic intermetallic particles and the matrix, whereby the potential difference causes the surrounding matrix to dissolve, leading to pitting[2,21]. In contrast, the corrosion path follows the grain boundaries in the T6 condition due to galvanic coupling of the microstructural features of the grain boundaries, such as grain boundary precipitates[2,10–14] or element enrichment[10,11,15,19,20] with the PFZ and/or SDZ[4,13–18]. The exact mechanisms remain highly dependent on the alloy composition, especially on the contents of Mg, Si, and Cu[24], or the exact thermomechanical history[10].

Despite the switch from pitting for the T4 condition to IGC for the T6 condition, the model still overpredicts the IGC conditions. This further reiterates the importance of microstructure when considering IGC of aluminum alloys. The role of microstructure has been explored in many alloy systems[57]. For aluminum alloys, there is conflicting information in the literature on the influence of grain size on the resulting corrosion rate. The effect of grain refinement to be considered as purely a "structural" change is an oversimplification in the context of aluminum systems[57].

Thus, the decrease in accuracy and performance of the developed framework is caused by the fact that the trained model needs to incorporate details regarding the microstructure and relevant physics adequately in order to capture pitting corrosion, as well as taking into account the path length and branching of the IGC corrosion attack. Therefore, by adequately enabling the model to distinguish and account for the corrosion mechanism, as well as integrating relevant information about the microstructure, better predictions will be obtained. This means that in order to obtain better predictions in scenarios where the corrosion mechanism is different or the grain sizes are more elongated, new features should be suitably incorporated into the input domain, such as details regarding the microstructure.

It is important to point out that the new microstructural features need to sufficiently capture relevant information about the underlying grain orientation, grain structure, as well as the morphology (i.e., grain shape and size) of the grains in order to enhance the predictions and train a microstructure-aware surrogate model. This initially involves extensive microstructural analysis, but offers the potential to provide missing information about the manufacturing process in the future. Successfully predicting uncertainties also makes it possible to design an appropriate experimental design in the future, as well as to serve as a foundation for data collection in self-driving labs. Nevertheless, it is important to recognize that overall, the developed framework successfully enabled the extraction of usable knowledge and, most importantly, it enabled the capability to utilize such knowledge effectively and efficiently for new/unseen alloys.

Methods

Experimental details

For the development of a prediction tool for the penetration depth of intergranular corrosion based on a machine learning approach, the penetration depths of the alloys shown in Table 4, which were previously published, were considered. With the exception of alloy AA6056 (wire material with diameters of either 10.25 or 8 mm[2–4,13,42]), these are sheet materials with thicknesses of approximately 1 mm[29,30]. The selected sheet and wire samples exhibited predominantly equiaxed grain morphologies of similar sizes. The heat treatment conditions considered can be designated as either solution-annealed and quenched (T4), bake-hardened (BH), or peak-aged (T6).

As a blind test, three industrially produced and heat-treated model alloys with varying Cu contents were investigated in the T4 and T6 conditions with a sheet thickness of 2 mm. Additionally, results from sheet materials in T6 condition, which have been previously published, with a thickness of approximately 2 mm, were also considered for blind testing the model[8,9]. The relevant contents of the main alloying elements Mg, Si, and Cu can also be found in Table 4. With the exception of the solution annealing parameters for alloys 6014 and 6016, which are subject to a confidentiality agreement with industry partners, the heat treatment parameters can be found in the relevant references. For the sake of consistency, the heat treatment conditions have been implemented as categorical values. However, for an independent validation, also of the blind test alloys, we refer to the comprehensive heat treatment parameters specified by Mueller et al.[8,9]. The alloys used for model development, training, and the blind test are shown in Fig. 7 for classification within the 6000 series with their Mg/Si vs. Cu and Mg vs. Si contents. The blue boxes indicate the chemical composition window of the alloys in the area of interest. The alloy designations have been carried over from the respective reference to the corresponding data points, and some data points may deviate from the standard alloy specification given in ref. 58. This applies to the alloy composition of 6014, visible in Fig. 7b. Furthermore, the stoichiometric composition limit of the Mg_2Si equilibrium phase is shown, which marks the transition to the undesirable excess Mg region[54,59]. The dashed lines indicate the limits of a positive intermediate storage effect[60] and Mg_2Si solubility[59].

The IGC susceptibility of the model alloys is tested according to EN ISO 11846 method B[31], taking into account the standard test parameters defined by Zander et al.[29]. The samples are first cut to a size of 29 mm × 49 mm and then pickled in 5% NaOH solution at 50 °C for 2 min, followed by immersion in an aqueous solution of 30 g/l NaCl and 10 ml

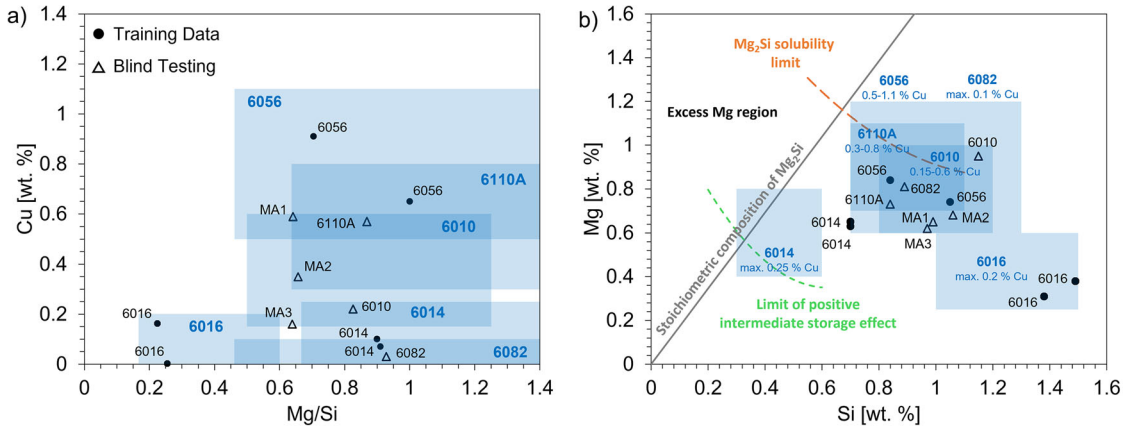

Fig. 7 | Alloying content figures for the curated database and the unseen conditions. Classification of used alloys for model development and unseen conditions testing related to **a** Mg/Si vs. Cu and **b** Si vs. Mg content within the 6000 series designation system[2,3,8,9,29,30]. Blue boxes indicate the chemical composition range according to the specification in the teal sheets[58]. The model alloys (MA's) are marked as MA1–MA3.

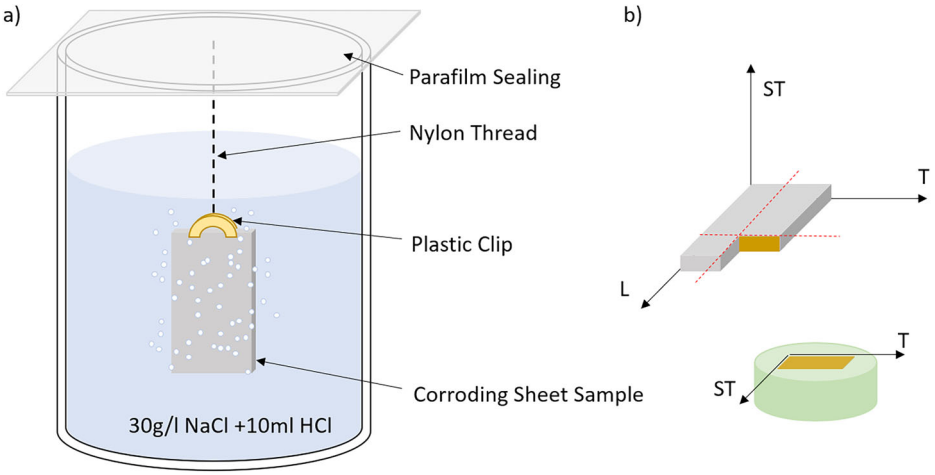

Fig. 8 | Schematic of the experimental setup used in this work. a Schematic experimental setup as previously used for IGC testing according to ISO EN 11846 Method B. **b** Metallographic cross-section preparation sites dependent on analyzing the penetration depth in longitudinal (L), transverse (T), and short-transverse (ST) directions.

concentrated HCl (37%) for 24 h. The surface-to-volume ratio is set to 5 ml/cm^2 in order to equalize the influence of the sample size, which may be between 4 and 20 ml/cm^2 according to EN ISO 11846 Method B. The samples are immersed in beakers using a chemical-resistant, nonconductive plastic clamp and a nylon thread so that the surface is almost completely wetted. The beakers are then shielded from the environment with Parafilm® and placed in a water bath at a constant temperature of 30 °C. Schematically, the set-up is visible in Fig. 8a.

Following the immersion test, samples are rinsed in distilled water and dried. Metallographic cross-sections of three samples per condition are then prepared. The penetration depth of the intergranular corrosion attack is measured in the ST × T plane (Fig. 8b) using optical light microscopy. The maximum penetration depth of each sample is calculated as the average of the five largest penetration depths. Microstructure characterization of the materials in T4 condition was performed by Barker etching samples of each sheet direction and taking images using an optical light microscope. The Barker etching was performed for 80 s at a potential of 20 V[50].

Additionally, electron back-scatter diffraction (EBSD) measurements were performed on the ST × L plane of blind test alloys using a Gemini Ultra 55VP SEM (Carl Zeiss Microscopy, Germany) equipped with an EBSD detector from Oxford Instruments, UK. EBSD maps were collected with a step size of 2 µm and an electron acceleration voltage of 20 kV. The AZtecCrystal 2.0 software was used for data evaluation. This provided insights into the grain aspect ratio of the high-angle grain boundaries, as it allows for the differentiation between various types of grain boundaries based on the misorientation angles of the grain boundaries in the most elongated plane. Whereby low-, medium-, and high-angle grain boundaries have been assigned to a misorientation angle of <5 °, 5°−15°, and >15°, respectively.[52]

Data availability

The data generated and analyzed are not publicly available due to a confidentiality agreement, but can be made available upon reasonable request to the first author or the corresponding author.

Code availability

The codes used to generate the results in this study are not publicly available due to an ongoing study but can be made available upon reasonable request to the first author or the corresponding author.

Received: 18 August 2026; Accepted: 14 October 2026;
Published online: 15 November 2026

References

1. Gao, Y.-C. et al. Research progress, application and development of high performance 6000 series aluminum alloys for new energy vehicles. *J. Mater. Res. Technol.* **32**, 1868–1900 https://doi.org/10.1016/j.jmrt.2024.08.018 (2024).
2. Zander, D., Schnatterer, C., Altenbach, C. & Chaineux, V. Microstructural impact on intergranular corrosion and the mechanical

properties of industrial drawn 6056 aluminum wires. *Mater. Des.* **83**, 49–59 (2015).
3. Schnatterer, C., Altenbach, C. & Zander, D. The effect of simulated in-service heat impact on the microstructure and corrosion properties of a high Cu containing Al-Mg-Si alloy. *Mater. Corros.* **70**, 1205–1213 (2019).
4. Schnatterer, C. *Interkristalline Korrosion und Spannungsrisskorrosion von Al-Mg-Si-Cu-Drähten* (Shaker Verlag, 2018).
5. Avramenko, T. et al. Review on environmentally assisted static and fatigue cracking of Al-Mg-Si-(Cu) alloys. *Metals* **14**, 621 (2024).
6. Altenbach, C. et al. *Korrosionsmechanismen von Aluminiumknetlegierungen, Abhängigkeiten von Legierungselementen und Prozessen am Beispiel der Interkristallinen Korrosion Verstehen und Prüfen*. Presentation at the ASMET Automobiltagung (2022).
7. Katona, R. M., Karasz, E. K. & Schaller, R. F. A review of the governing factors in pit to crack transitions of metallic structures. *Corrosion* **79**, 72–9611 https://doi.org/10.5006/4179 (2023).
8. Müller-Jena, R. et al. The effect of deformation mode and microstructure on the IGC susceptibility of Al-Mg-Si-Cu alloys for automotive applications. In: *Light Metals* (Springer, 2020) pp. 352–361.
9. Müller-Jena, R., Springer, H. J. & Zander, B. D. *Einfluss von Kalt-und Warmumformprozessen auf die lokalen Korrosionsmechanismen von Al-Mg-Si-Cu-Legierungen* (Lehrstuhl für Korrosion und Korrosionsschutz, 2022).
10. Svenningsen, G., Larsen, M. H., Nordlien, J. H. & Nisancioglu, K. Effect of thermomechanical history on intergranular corrosion of extruded AlMgSi (Cu) model alloy. *Corros. Sci.* **48**, 3969–3987 (2006).
11. Bhattamishra, A. K. & Lal, K. Influence of ageing on corrosion behaviour of Al-Mg-Si alloys in chloride and acid media. *Int. J. Mater. Res.* **89**, 793–796 (2021).
12. Larsen, M. H., Walmsley, J. C., Lunder, O., Mathiesen, R. H. & Nisancioglu, K. Intergranular corrosion of copper-containing aa6xxx almgsi aluminum alloys. *J. Electrochem. Soc.* **155**, C550 (2008).
13. Schnatterer, C., Bulinger, A. & Zander, D. Evaluating the intergranular corrosion susceptibility of Al-Mg-Si-Cu alloys using electrochemical methods. *Mater. Corros.* **67**, 1308–1313 (2016).
14. Svenningsen, G. et al. Effect of low copper content and heat treatment on intergranular corrosion of model AlMgSi alloys. *Corros. Sci.* **48**, 226–242 (2006).
15. Holmestad, J., Ervik, M., Marioara, C. D. & Walmsley, J. C. Investigation of grain boundaries in an Al-Mg-Si-Cu alloy. *Mater. Sci. Forum* **794**, 951–956 (2014).
16. Larsen, M. H., Walmsley, J. C., Lunder, O. & Nisancioglu, K. Effect of excess silicon and small copper content on intergranular corrosion of 6000-series aluminum alloys. *J. Electrochem. Soc.* **157**, C61 (2009).
17. Li, H. et al. The intergranular corrosion susceptibility of a heavily overaged Al-Mg-Si-Cu alloy. *Corros. Sci.* **107**, 113–122, https://doi.org/10.1016/j.corsci.2016.02.025 (2016).
18. Shi, A., Shaw, B. & Sikora, E. The role of grain boundary regions in the localized corrosion of a copper-free 6111-like aluminum alloy. *Corrosion* **61**, 534–547 (2005).
19. Bhattamishra, A. & Lal, K. Microstructural studies on the effect of Si and Cr on the intergranular corrosion in Al-Mg-Si alloys. *Mater. Des.* **18**, 25–28 (1997).
20. Svenningsen, G., Larsen, M. H., Walmsley, J. C., Nordlien, J. H. & Nisancioglu, K. Effect of artificial aging on intergranular corrosion of extruded aAlMgSialloy with small cu content. *Corros. Sci.* **48**, 1528–1543 (2006).
21. Adapala, P. et al. Understanding the effect of microstructure and composition on localized corrosion susceptibility of 6xxx aluminum alloys. *npj Mater. Degrad.* **8**, 52 (2024).
22. Kumari, S., Wenner, S., Walmsley, J. C., Lunder, O. & Nisancioglu, K. Progress in understanding initiation of intergranular corrosion on aa6005 aluminum alloy with low copper content. *J. Electrochem. Soc.* **166**, C3114–C3123 (2019).
23. Zou, Y. et al. The intergranular corrosion behavior of 6000-series alloys with different Mg/Si and Cu content. *Appl. Surf. Sci.* **405**, 489–496 (2017).
24. Kairy, S., Rometsch, P., Davies, C. & Birbilis, N. On the intergranular corrosion and hardness evolution of 6xxx series Al alloys as a function of Si: Mg ratio, Cu content, and aging condition. *Corrosion* **73**, 1280–1295 (2017).
25. Kairy, S. K. et al. Understanding the origins of intergranular corrosion in copper-containing Al-Mg-Si alloys. *Metall. Mater. Trans. A* **47**, 985–989 (2016).
26. ichi Ikeda, K. et al. Effects of scandium and zirconium addition on recrystallization behavior of Al-Mg-Si alloy. *Mater. Trans.* **59**, 590–597 https://doi.org/10.2320/matertrans.L-M2018802 (2018).
27. Guemini, R., Boubertakh, A. & Lorimer, G. W. Study of the recrystallization process of AlMgSi alloys containing transition elements. *J. Alloy. Compd.* **486**, 451–457 (2009).
28. Sari, I. A., Ozcelik, G. & Yucel, O. Impact of v additions on the microstructure and mechanical properties of al-6xxx alloy. *Can. Metall. Q.* **64**, 1886–1895 (2025).
29. Cornejo, M. et al. Intergranular corrosion testing of 6000 aluminum alloys. *Mater. Corros.* **69**, 626–633 (2018).
30. Cornejo, M. et al. A comparison of accelerated corrosion tests for the assessment of the intergranular corrosion susceptibility of bare 6000 aluminum sheets. *Mater. Corros.* **70**, 623–632 (2019).
31. für Normung e.V., D. I. Corrosion of metals and alloys—determination of resistance to intergranular corrosion of solution heat-treatable aluminum alloys (ISO 11846:1995 (2008).
32. LeCun, Y., Bengio, Y. & Hinton, G. Deep learning. *nature* **521**, 436–444 (2015).
33. Montes de Oca Zapiain, D. et al. Accelerating fem-based corrosion predictions using machine learning. *J. Electrochem. Soc.* **171**, 011504 (2024).
34. Venkatraman, A. et al. An active learning framework for the rapid assessment of galvanic corrosion. *npj Mater. Degrad.* **8**, 54 (2024).
35. Coelho, L. B. et al. Reviewing machine learning of corrosion prediction in a data-oriented perspective. *npj Mater. Degrad.* https://doi.org/10.1038/s41529-022-00218-4 (2022).
36. Ma, S., Du, Y., Wang, S. & Su, Y. Application of machine learning in material corrosion research. *Corros. Rev.* https://doi.org/10.1515/corrrev-2022-0089 (2023).
37. Li, J. et al. Synergistic enhancement of strength and corrosion resistance in Al-Mg-Si alloys through chemical composition design via machine learning approaches. *Mater. Design* 115310 (2025).
38. Feng, X., Wang, Z., Jiang, L., Zhao, F. & Zhang, Z. Simultaneous enhancement in mechanical and corrosion properties of Al-Mg-Si alloys using machine learning. *J. Mater. Sci. Technol.* **167**, 1–13 (2023).
39. Sheik, S., Mohammed, R., Teeparthi, K. & Raghuvamsi, Y. Machine learning-based prediction of intergranular corrosion resistance in austenitic stainless steels exposed to various heat treatments. *J. Inst. Eng. (India)* **106**, 491–504 (2025).
40. Falaakh, D. F. & Bahn, C. B. Machine learning for modeling intergranular stress corrosion cracking of stainless steels in light water reactors with uncertainty quantification and explainability. *npj Mater. Degrad.* (2025).
41. Schapire, R. E. et al. A brief introduction to boosting. *Ijcai* **99**, 1401–1406 (1999).
42. Schnatterer, C. & Zander, D. Influence of the grain boundary chemistry on the intergranular corrosion mechanisms of a high-strength Al-Mg-Si alloy. *Surf. Interface Anal.* **48**, 750–754 (2016).
43. Venkatraman, A., Katona, R. M. & Montes de Oca Zapiain, D. Matse-multi-fidelity augmented time-series emulation: galvanic corrosion applications. *Mach. Learn.* **6**, 025031 (2025).

44. Williams, C. & Rasmussen, C. Gaussian processes for regression. *Adv. Neural Inf. Process. Syst.* **8** (1995).
45. Kramer, O. Scikit-learn. In: *Machine Learning for Evolution Strategies*. (Springer, 2016), pp. 45–53.
46. Goldberg, P., Williams, C., & Bishop, C. Regression with input-dependent noise: a Gaussian process treatment. *Adv. Neural Inf. Process. Syst.* **10** (1997).
47. Le, Q. V., Smola, A. J. & Canu, S. Heteroscedastic Gaussian process regression. In: *Proceedings of the 22nd International Conference on Machine Learning*, pp. 489–496 (2005).
48. Matthews, A. G.dG. et al. Gpflow: A Gaussian process library using TensorFlow. *J. Mach. Learn. Res.* **18**, 1–6 (2017).
49. Joliffe, I. T. & Morgan, B. Principal component analysis and exploratory factor analysis. *Stat. Methods Med. Res.* **1**, 69–95 (1992).
50. Barker, L. Revealing the grain structure of common aluminum alloy metallographic specimens. *Trans. ASM* **42**, 347 (1950).
51. Kahrıman, F. & Zeren, M. Determination of activation energy for static recrystallization in Al-Mg-Si alloys with different Zr contents. *Key Eng. Mater.* **951**, 33–46 (2023).
52. Lervik, A., Wenner, S., Lunder, O., Marioara, C. & Holmestad, R. Grain boundary structures and their correlation with intergranular corrosion in an extruded Al-Mg-Si-Cu alloy. *Mater. Charact.* **170**, 110695 (2020).
53. Mukhopadhyay, P. Alloy designation, processing, and use of aa6xxx series aluminium alloys. *Int. Sch. Res. Not.* **2012**, 165082 https://doi.org/10.5402/2012/165082 (2012).
54. Mondolfo, L. Structure and properties. *Aluminum Alloys* **518** (1976).
55. Frankel, G. S. Pitting corrosion of metals. A review of the critical factors. *J. Electrochem. Soc.* **145**, 2186–2198 https://doi.org/10.1149/1.1838615 (1998).
56. Kairy, S. K. et al. Exploring the electrochemistry of 6xxx series aluminium alloys as a function of Si to Mg ratio, Cu content, ageing conditions and microstructure. *Electrochim. Acta* **190**, 92–103 https://doi.org/10.1016/j.electacta.2015.12.098 (2016).
57. Ralston, K. D. & Birbilis, N. Effect of grain size on corrosion: a review. *Corrosion* **66**, 075005–1–075005–13 https://doi.org/10.5006/1.3462912 (2010).
58. Inc., T. A. A. *International Alloy Designations and Chemical Composition Limits for Wrought Aluminum and Wrought Aluminium Alloys* (2025).
59. Altenpohl, D. *Aluminium und Aluminiumlegierungen* (Springer, Berlin, Heidelberg, 1965).
60. Zoller, H. & Ried, A. Metallkundliche gesichtspunkte bei der entwicklung wenig abschreckempfindlicher almgsi-legierungen/metallurgical aspects in the development of almgsi alloys with a low sensitivity to quenching. *Int. J. Mater. Res.* **62**, 354–358 (1971).

Acknowledgements

The authors would like to acknowledge Stefanie D¨uker and Rahul Thomas Kurian for their support with the experimental work. Sandia National Laboratories is a multi-mission laboratory managed and operated by National Technology and Engineering Solutions of Sandia, LLC, a wholly owned subsidiary of Honeywell International, Inc., for the U.S. Department of Energy National Nuclear Security Administration under contract DE-NA0003525. This paper describes objective technical results and analysis. Any subjective views or opinions that might be expressed in the paper do not necessarily represent the views of the U.S. Department of Energy or the United States Government.

Author contributions

David Montes de Oca Zapiain: Conceptualization, Data curation, Investigation, Methodology, Validation, Visualization, Writing – original draft, Writing – review and editing; Christoph Altenbach: Conceptualization, Data curation, Investigation, Methodology, Validation, Writing – original draft, Writing - Review & Editing, Visualization Laura Kopruch: Conceptualization, Data curation, Validation, Investigation, Writing - Review & Editing, Visualization Ryan M. Katona: Conceptualization, Visualization, Writing – original draft, Writing – review and editing, Resources, Funding; Aditya Venkatraman: Conceptualization, Methodology, Writing – review andediting; Daniela Zander: Resources, Writing - Review & Editing.

Funding

The authors received no specific funding for this work.

Competing interests

The authors declare no competing interests.

Additional information

Correspondence and requests for materials should be addressed to David Montes de Oca Zapiain.

Reprints and permissions information is available at http://www.nature.com/reprints

Publisher's note Springer Nature remains neutral with regard to jurisdictional claims in published maps and institutional affiliations.

Open Access This article is licensed under a Creative Commons Attribution-NonCommercial-NoDerivatives 4.0 International License, which permits any non-commercial use, sharing, distribution and reproduction in any medium or format, as long as you give appropriate credit to the original author(s) and the source, provide a link to the Creative Commons licence, and indicate if you modified the licensed material. You do not have permission under this licence to share adapted material derived from this article or parts of it. The images or other third party material in this article are included in the article's Creative Commons licence, unless indicated otherwise in a credit line to the material. If material is not included in the article's Creative Commons licence and your intended use is not permitted by statutory regulation or exceeds the permitted use, you will need to obtain permission directly from the copyright holder. To view a copy of this licence, visit http://creativecommons.org/licenses/by-nc-nd/4.0/.

© The Author(s) 2026

This Article in Press is shared early to give you faster access to new research. It is citable and carries a permanent DOI. The final edited version will replace it automatically.